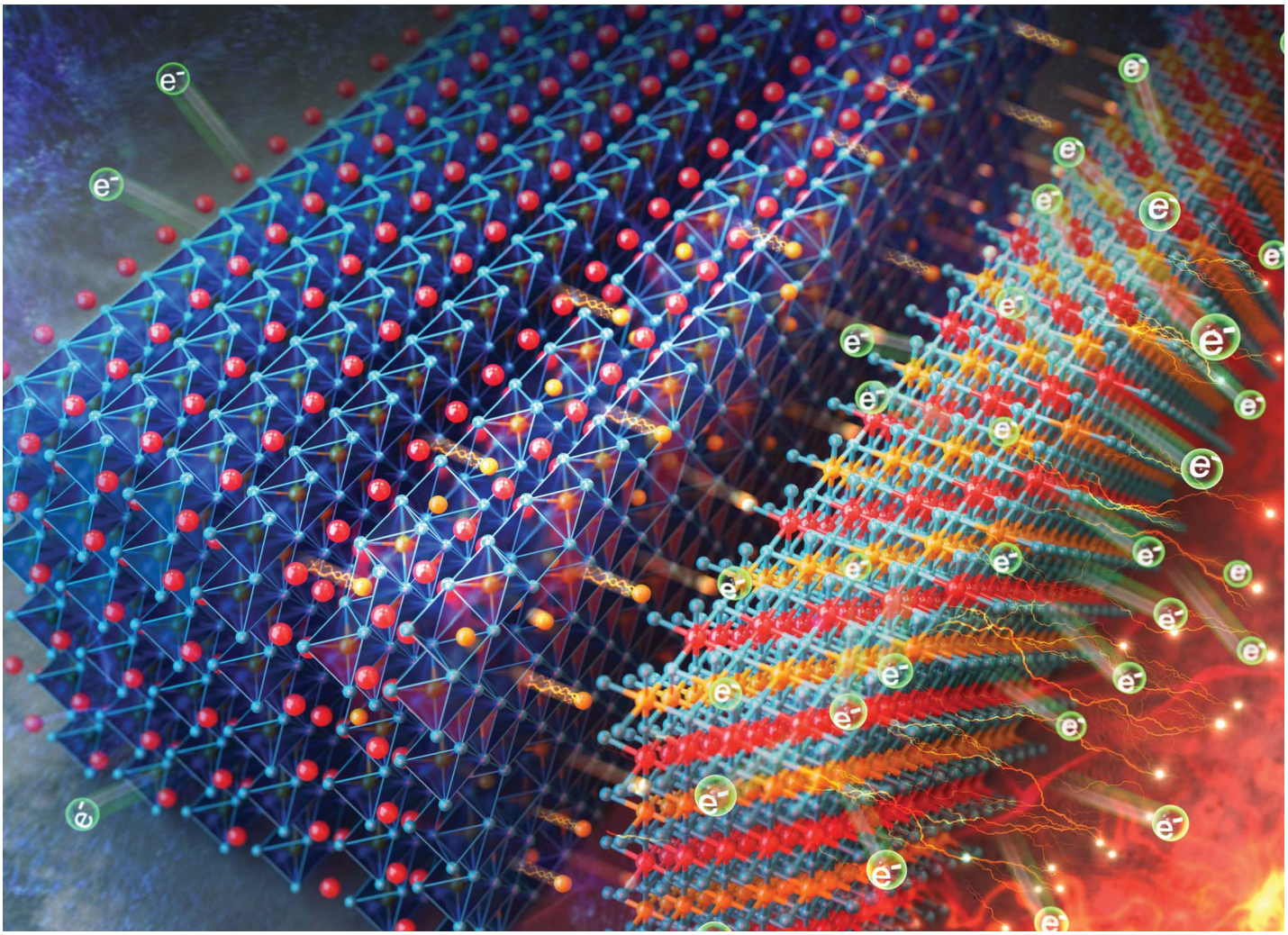

Highlighting a study on the band nestification of $AgBiSe_2$-$CuBiSe_2$ by a group of researchers led by Prof. Yeon Sik Jung from Korea Advanced Institute of Science and Technology and Prof. Min-Wook Oh from Hanbat National University.

Order-disorder transition-induced band nestification in $AgBiSe_2$–$CuBiSe_2$ solid solutions for superior thermoelectric performance

Environmentally benign $AgBiSe_2$-$CuBiSe_2$ solid solutions are demonstrated as high-performance thermoelectric materials. By incorporating Cu atoms into Ag sites, multiple electronic bands are formed at an identical K point, abruptly increasing the weighted mobility of the material.

As featured in:

See Yeon Sik Jung, Min-Wook Oh *et al.*, *J. Mater. Chem. A*, 2021, **9**, 4648.

ROYAL SOCIETY OF CHEMISTRY

rsc.li/materials-a

Registered charity number: 207890

Journal of Materials Chemistry A

ROYAL SOCIETY OF CHEMISTRY

COMMUNICATION

View Article Online
View Journal | View Issue

Cite this: J. Mater. Chem. A, 2021, 9, 4648

Received 29th August 2020
Accepted 30th November 2020

DOI: 10.1039/d0ta08484k

rsc.li/materials-a

Order-disorder transition-induced band nestification in $AgBiSe_2$–$CuBiSe_2$ solid solutions for superior thermoelectric performance†

Hanhwi Jang,[a] Stanley Abbey,[b] Woo Hyun Nam,[c] Brakowaa Frimpong,[b] Chien Viet Nguyen,[d] Sung-Jae Joo,[e] Ho Sun Shin,[d] Jae Yong Song,[d] Eugene N. Cho,[f] Moohyun Kim,[a] Yeon Sik Jung *[a] and Min-Wook Oh *[b]

Despite the fact that research into most high-performance thermoelectric (TE) materials is focused on tellurides, compelling demand has arisen to replace tellurium (Te) with selenium (Se) due to the scarcity of Te. Silver bismuth diselenide ($AgBiSe_2$, ABS) has been widely studied in relation to thermoelectric applications due to its intrinsically low thermal conductivity. However, its low power factor (PF) has been considered as an underlying issue preventing improvements of the TE properties of ABS. Here, it is demonstrated that a high PF can be achieved by incorporating Cu into the ABS system *via* the nestification of conduction bands when a disordering between Ag and Bi occurs. Degenerate electronic bands simultaneously increase the density-of-states effective mass and carrier concentration while not reducing the carrier mobility significantly. Therefore, improved TE performance with a maximum PF of 8.2 $\mu W\ cm^{-1}\ K^{-2}$ and a peak zT value of 1.14 was achieved at 773 K, opening a new horizon for the development of environmentally benign TE materials with high performance capabilities.

Thermoelectric (TE) energy conversion has attracted significant attention as a prospective sustainable power source featuring direct conversion from heat to electrical energy without mechanical parts.[1,2] However, because the low conversion efficiency hinders the market growth of this technology, most research focuses on improving the performance of TE materials. The conversion efficiency of the TE material is directly proportional to the dimensionless figure of merit ($zT = S^2\sigma T/\kappa$, where S is the Seebeck coefficient, σ is the electrical conductivity, T is the absolute temperature, and κ is the thermal conductivity of the TE material). From the equation, it is clear that increasing S and σ while decreasing κ results in a TE material with a high zT value.

Previous studies of TE materials highly focused on tellurides such as Bi_2Te_3,[3–5] GeTe,[6,7] SnTe,[8–10] $AgSbTe_2$,[11–14] Cu_2Te,[15–17] $Sb_2Si_2Te_6$,[18] and PbTe[19,20] due to their high TE performance capabilities.[21] However, it is imperative to seek an alternative to tellurium (Te) considering its scarcity in the earth's crust, which limits material availability compared to supply and threatens potential market growth of TE materials.[22] The development of selenium-based TE materials such as SnSe[23,24] and Cu_2Se[25,26] has been reported as part of the effort to replace Te. However, despite the few examples of polycrystalline SnSe which exhibited high performance,[27,28] SnSe often has high zT values in single crystals that are neither scalable nor mechanically robust,[29] while Cu_2Se has electromigration issues during high-current operation due to the presence of mobile Cu^+ ions.[30] Therefore, it is necessary to develop high-performance polycrystalline selenides with stable TE properties.

Silver-based ABX_2-type chalcogenides has gained considerable attention as it can replace conventional lead chalcogenide-based materials.[31–33] Among them, silver bismuth diselenide ($AgBiSe_2$, ABS) has been extensively studied as a thermoelectric material due to its intrinsically low thermal conductivity close to the amorphous minimum.[34–39] Lone-pair electrons (LPEs) in the 6s orbital of Bi greatly reduce the lattice thermal conductivity by intensifying the degree of lattice anharmonicity, which is highly favorable when developing high-performance TE materials.[40] However, the relatively low electrical conductivity (~30 S cm^{-1} at 700 K[37]) compared to that of the state-of-the-art thermoelectric materials results in a poor power factor (PF = $S^2\sigma$), which hinders the realization of a high zT value. Although efforts have

[a]Department of Materials Science and Engineering, Korea Advanced Institute of Science and Technology (KAIST), 291 Daehak-ro, Yuseong-gu, Daejeon, 34141, Republic of Korea. E-mail: ysjung@kaist.ac.kr

[b]Department of Materials Science and Engineering, Hanbat National University, 125 Dongseodae-ro, Yuseong-gu, Daejeon, 34158, Republic of Korea. E-mail: mwoh@hanbat.ac.kr

[c]Energy Efficiency Materials Center, Korea Institute of Ceramic Engineering and Technology (KICET), Jinju, 52851, Republic of Korea

[d]Korea Research Institute of Standards and Science (KRISS), Daejeon, 34113, Republic of Korea

[e]Energy Conversion Research Center, Korea Electrotechnology Research Institute (KERI), Changwon, 51543, Republic of Korea

[f]KAIST Institute for NanoCentury, Korea Advanced Institute of Science and Technology (KAIST), 291 Daehak-ro, Yuseong-gu, Daejeon, 34141, Republic of Korea

† Electronic supplementary information (ESI) available. See DOI: 10.1039/d0ta08484k

been made to improve the electrical conductivity of ABS by increasing the carrier concentration, an accompanying drop in the Seebeck coefficient greatly limits PF to a certain threshold.[36,37] For example, even when the carrier concentration is optimized, the reported maximum PF is approximately 5.5 $\mu W\ cm^{-1}\ K^{-2}$ for halogen-doped ABS.[37] Considering that the window in which to suppress the lattice thermal conductivity is significantly narrow, improving the electronic properties is required to increase the zT values of ABS.

Band convergence or band nestification of TE materials has been considered as a promising strategy to increase PF given that one can achieve a high Seebeck coefficient without diminishing the electrical conductivity.[41–46] Previous studies widely report that isovalent dopants can induce band convergence. Examples include $(Bi,Sb)_2Te_3$,[47] Pb(Se,Te),[41] $Mg_2(Si,Sn)$,[48] and $Mg_3(Sb,Bi)_2$.[43] For instance, isovalent doping on either the Bi sites[36,49] or Se sites[35,50,51] in ABS has already been conducted, though it was found to be ineffective to induce band convergence. Even though it was expected that Cu can induce valence band convergence in hexagonal structure by DFT calculations,[52] the effect of replacing Ag sites with group 11 elements (Cu and Au) has not been experimentally explored. Given the cost-effectiveness and earth-abundance of Cu compared to Au, we were motivated to investigate the transport properties of the $CuBiSe_2$-alloyed $AgBiSe_2$ (CABS) system.

Although various isovalent dopants have been introduced into the ABS matrix, maximum zT value has stagnated to approximately 0.6 at 773 K despite the corresponding low lattice thermal conductivity (Fig. 1a).[35,49,51] CABS alloys with low Cu concentrations also exhibit similar zT values resulting from the low μ_w values of the materials. However, an abrupt increase of μ_w starting from 500 K in CABS-27 ($Cu_{0.27}Ag_{0.73}BiSe_2$) greatly improves the zT value to 1.14 at 773 K, which surpasses the common threshold of isovalent-doped ABS. A temperature-dependent Pisarenko analysis in Fig. 1b reveals that the density-of-states effective mass (m^*_{DOS}) of CABS-27 becomes larger than that of other CABS alloys starting at 523 K, where ABS experiences a structural transition to a disordered cubic phase. Furthermore, it is now known that superior electronic properties in CABS-27 stem from the increase of the DOS effective mass, which is typically determined by $m^*_{DOS} = {N_v}^{3/2} m^*_b$, where N_v represents valley degeneracy and m^*_b is the band effective mass.[53] If a heavy DOS effective mass originates from a high m^*_b value, the electron mobility would be reduced and would prevent the achievement of a high PF. However, measured Hall mobility values at high temperatures do not change significantly in the CABS-27 system, implying that the increase of the DOS effective mass stems from an increase in valley degeneracy, not from m^*_b. (Fig. 1c).

It is known that the weighted mobility is expressed by following equation:

$$\mu_w = \mu_0 \left(\frac{m^*_{DOS}}{m_e}\right)^{3/2} = \mu_0 {N_v}^{3/2} \left(\frac{m^*_b}{m_e}\right)^{3/2},$$

where m_e is the electron mass, and μ_0 is the mobility of a carrier at k_BT higher than the band edge. The weighted mobility, an indicator of superior electronic properties yet independent of the carrier concentration, for the CABS alloys and pristine ABS clearly proves that the improvement does not come from only carrier concentration tuning but is indeed a beneficial effect of the increased N_v. While most ABS alloys exhibit a drastic drop of the weighted mobility at a high temperature, CABS-27 shows a persistent increase. Therefore, from a larger m^*_{DOS} and μ_w than that of other CABS alloys, one can infer that CABS-27 have higher N_v than that of other CABS alloys.

The BSE image of CABS-27 presented in Fig. 2a with EDX elemental mapping confirms a homogeneous distribution of elements without secondary phases on the micrometer scale. The room-temperature X-ray diffraction pattern reveals that CABS alloys crystallize in a hexagonal phase with a space group of $P\bar{3}m1$ (Fig. 2b). From the HRTEM image, the typical layered crystal structure of ABS with high crystallinity is found, meaning that the structure is well preserved upon Cu alloying. This layered structure enters one of two cubic phases, the $L1_1$ (AF-II) structure or the $D4$ (AF-IIb) structure at high temperatures, which represents disordering of cations between Ag and Bi atoms, as described in Fig. 2f.[54] One can notice that the AF-II ($L1_1$) structure with alternating Ag, Se, and Bi planes normal to the [111] direction can be obtained by rotating the second and fourth plane of the AF-IIb ($D4$) structure by 90° around the z axis.[55] However, these structures are not able to be distinguished with X-ray diffraction as both of them have characteristic Ag–Se–Bi–Se… chains in all periodic directions. Therefore, it is possible only to capture the cubic transition from the hexagonal structure by observing the decrease in the number of reflections (Fig. 2c). The phase transition also affects the valence state of the elements, as confirmed by *in situ* XPS results (Fig. S1†). Furthermore, the Hall carrier concentration of CABS alloys greatly increases after the phase transition (Fig. 2d). One should note that the electron concentration increases as more Cu incorporates into the ABS system. The disordering of cations on phase transition is shown in schematic diagram in Fig. 2e. Two distinctive crystallographic sites exist in the crystal structure of hexagonal ABS, and they possess different valence states for the neutral and 3+ conditions. In turn, the metallic Bi disappears and Bi^+ emerges after the phase transition; outcomes which may be related to the crystal structures of $L1_1$ and $D4$, as all Bi are assumed to share electrons with the nearest atoms. These mixed valence states of ABS would possibly form anisotropic bonding that diminishes the lattice thermal conductivity.[56–59]

Next, we explore the thermoelectric transport properties of CABS alloys. The Seebeck coefficients of CABS alloys at 323 K are nearly identical at approximately $-135\ \mu V\ K^{-1}$ due to their similar carrier concentrations (Fig. 3a). The deviation of the Seebeck coefficient of CABS-20 stems from the slightly lower carrier concentration, presumably due to the different defect concentrations. The total and lattice thermal conductivity levels at room temperature increased with additional alloying of Cu onto the ABS, which is opposite to what is expected from the Klemens alloy scattering model[60] (Fig. 3d and e). However, considering the increase of the average grain size, reduced phonon scattering at the grain boundary should be the

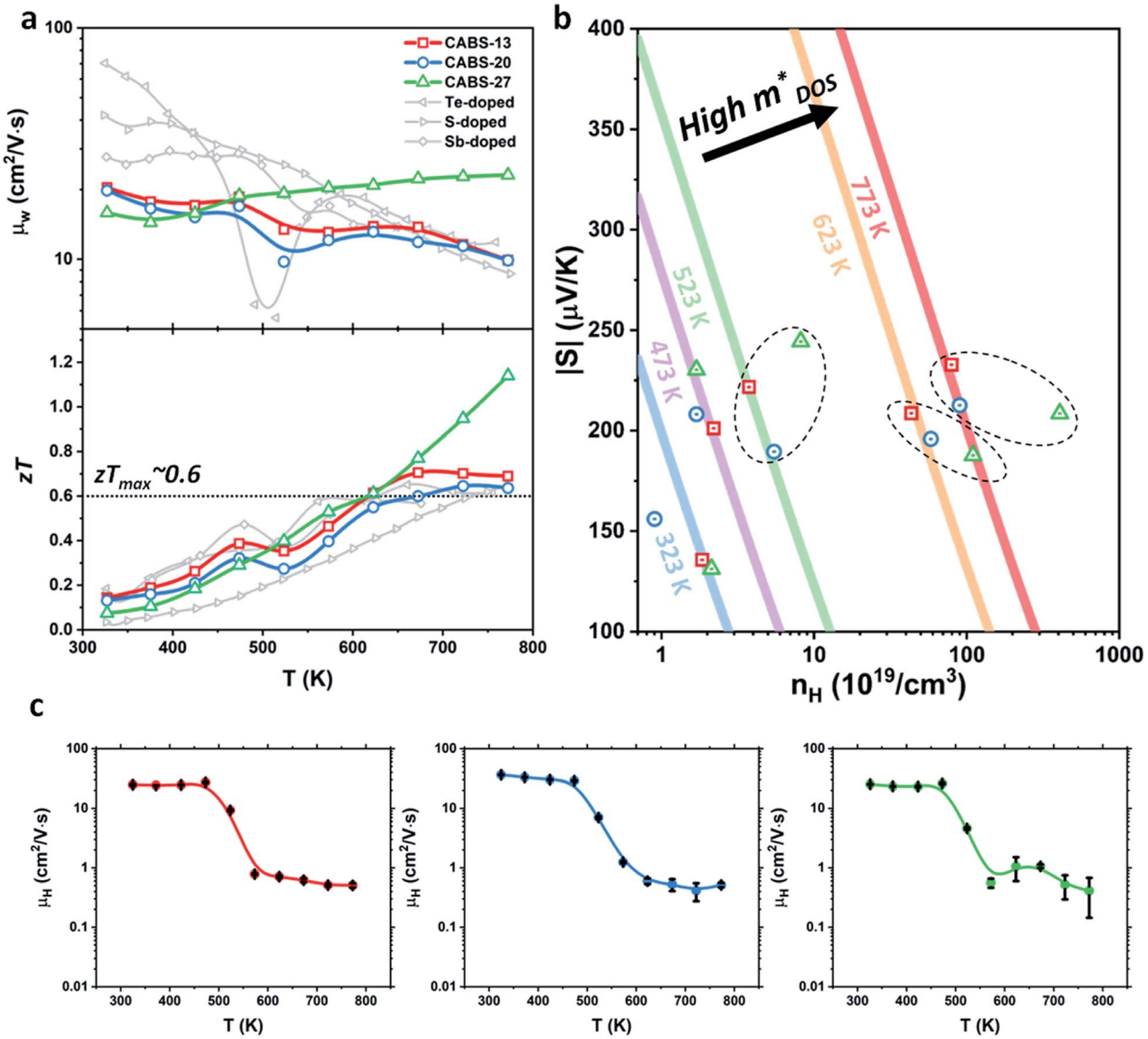

Fig. 1 Band nestification breaking the zT threshold of $AgBiSe_2$. (a) Comparison of the temperature-dependent weighted mobility (μ_w) and zT values of $AgBiSe_2$ alloyed with an isovalent element.[35,49,51] Most of the zT values converge to ~0.6, while CABS-27 exhibits a zT value of 1.14 at 773 K. (b and c) Temperature-dependent (b) Pisarenko plot and (c) Hall mobility showing the heavier m^*_{DOS} of CABS-27 compared to those of other CABS alloys despite relatively unchanged Hall mobility. Points in one circle are measured at the same temperature.

principal cause of the increased thermal conductivities at room temperature (see Fig. S2 and S3 in the ESI†). The increased grain size is attributed to the lowering of the melting point, which is also observed in the $Mg_3(Bi,Sb)_2$ system.[61] Moreover, it is found that the grain size also affects to the phase transition dynamics. The larger grain has a lower phase transition temperature compared to that of the smaller grain in the same composition (Fig. S17†).[62,63] For example, CABS-27 having bimodal distribution of the grain size has a shoulder peak at the transition temperature (Fig. S25†). The detailed discussion on the influence of grain size on the lattice thermal conductivity and DSC experiment can be found in the ESI.†

At high temperatures exceeding 600 K, the Seebeck coefficient of CABS alloys rises with the temperature, indicating degenerate conduction behavior. In addition, CABS alloys with high Cu concentrations exhibit lower Seebeck coefficients along with higher electrical conductivity. The calculated PF outcomes are similar for the three CABS alloys at temperatures of less than 450 K (Fig. 3c). Even at high temperatures, the PF values of CABS-13 and 20 do not exceed 4 μW cm^{-1} K^{-2}. However, the PF of CABS-27 rises sharply from 450 K, reaching 8.2 μW cm^{-1} K^{-2} at 773 K, which is more than double that of the PF values of the pristine sample and a 33% increase over that of halogen-doped ABS.[37]

As acoustic phonon scattering dominates at high temperatures,[64] the lattice thermal conductivity of CABS alloys typically has a similar value of 0.3 W m^{-1} K^{-1} with less of an effect of grain boundary scattering compared to that at room

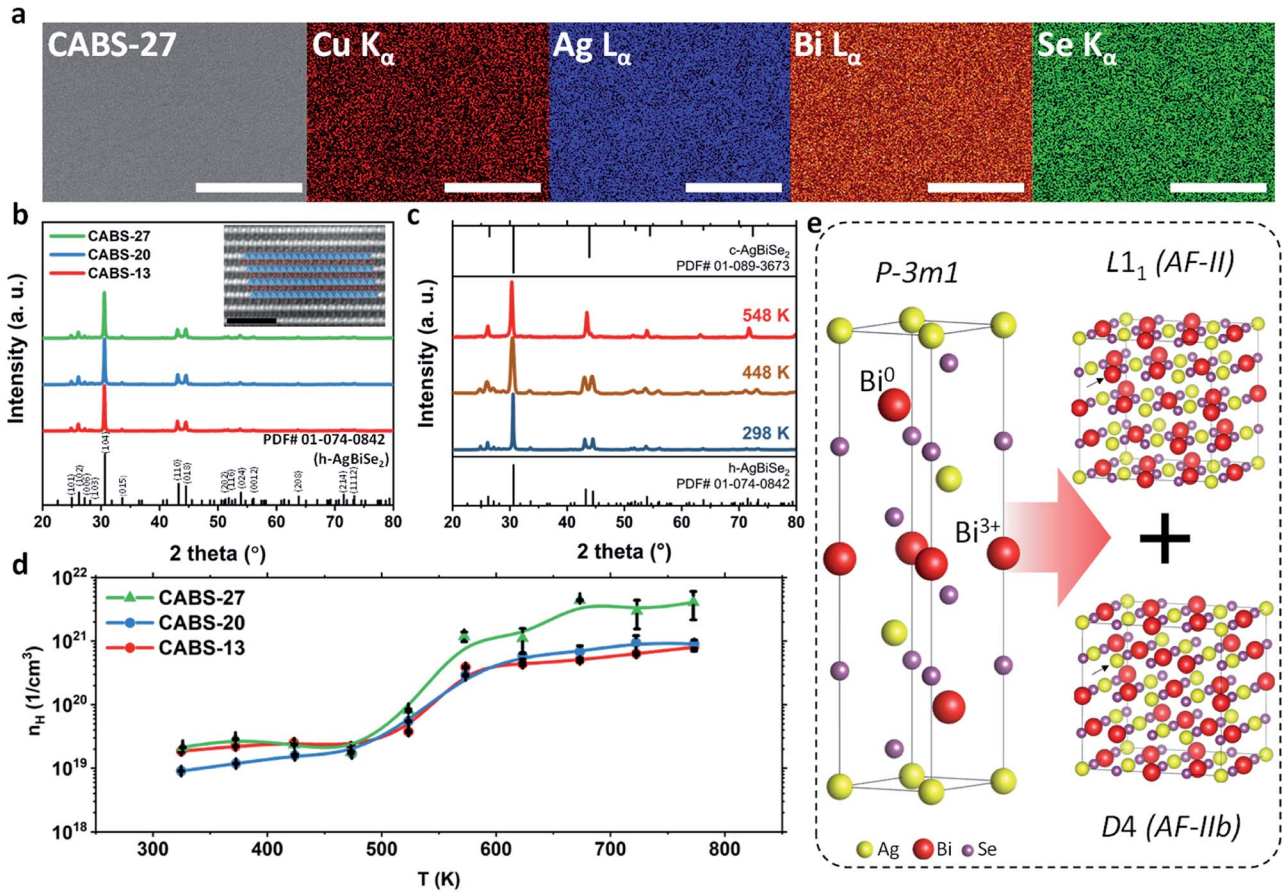

Fig. 2 Characterization of CABS alloys. (a) Representative BSE image of the polished surface of CABS-27 with EDX elemental mapping. Scale bar = 50 μm. (b) Room-temperature powder X-ray diffraction patterns of CABS alloys. The inset in (b) is a HRTEM image of CABS-27 with a schematic drawing of its layered crystal structure. Scale bar = 5 nm. (c) High-temperature powder X-ray diffraction pattern of CABS-27, showing a hexagonal-to-cubic phase transition upon heating. (d) Temperature-dependent Hall carrier concentration of CABS alloys. (e) Schematic drawing of the order-disorder transition in ABS upon heating. The difference in site substitution between Ag and Bi in the $L1_1$ and $D4$ supercell is depicted by the arrow.

temperature. A high zT value of 1.14 at 773 K is achieved for CABS-27 owing to the high PF combined with the low lattice thermal conductivity (Fig. 3f). Furthermore, CABS-27 exhibits superior performance not only in terms of zT_{max} but also with regard to zT_{avg} compared to other ABS-related TE materials (Fig. S4†).

To unveil the physical origin of improved PF of CABS-27, density functional theory (DFT) calculations of the electronic band structure are conducted. In this study, we consider the two situations of $L1_1$ and $D4$ structures. The electronic band structures of $Ag_{16}Bi_{16}Se_{32}$ (ABS), $Cu_1Ag_{15}Bi_{16}Se_{32}$ (CABS), and $Cu_{16}Bi_{16}Se_{32}$ (CBS) with the $L1_1$ structure are presented in Fig. 4a, b and c, respectively. It was found that cubic ABS with the $L1_1$ structure is a narrow-gap semiconductor with a band gap of 0.065 eV and valley degeneracy of 1. The calculated band gap is relatively small compared to the result of Hoang *et al.*, as the spin–orbit-interaction (SOI) tends to decrease the band gap, though it is crucial for evaluating a material with heavy elements.[65] The estimated band gap without SOI is 0.221 eV, which is almost half of the band gap calculated for HSE06 hybrid functionals (see Fig. S5 in the ESI†).[66] Considering that PBE calculations underestimate the band gap compared to hybrid calculations, our calculation results are in good agreement with the reported values.[67,68] The band gap is reduced to 0.043 eV in CABS, and it eventually closes, showing a pseudo-gap feature in CBS. It is expected that the effect of Cu on the band gap is significant in the cubic structure as opposed to the hexagonal structure, as we did not observe any significant difference in the band gap at room temperature (see Fig. S6 in the ESI†). Moreover, it is important to note that the relative positions of conduction bands are strongly affected by Cu, despite the fact that most of the states above the Fermi level in the $L1_1$ structure are mainly dominated by the Bi 6p orbital.[55,66] In fact, considering that Ag in the Ag–Se–Bi–Se–Ag–Se–Bi–Se… chain greatly perturbs the hybridization between Bi and Se, Cu can also manipulate the Bi–Se hybridization states and the conduction band.[55] A similar variation in the conduction band is observed in the $D4$ structure as well (see Fig. S7 in the ESI†).

Compared to ABS, it is apparent that a new conduction band near the conduction band minimum (CBM) at the T point is formed in CABS. As the Cu content increases, more conduction bands form near the CBM (see Fig. S16 in the ESI†). Finally,

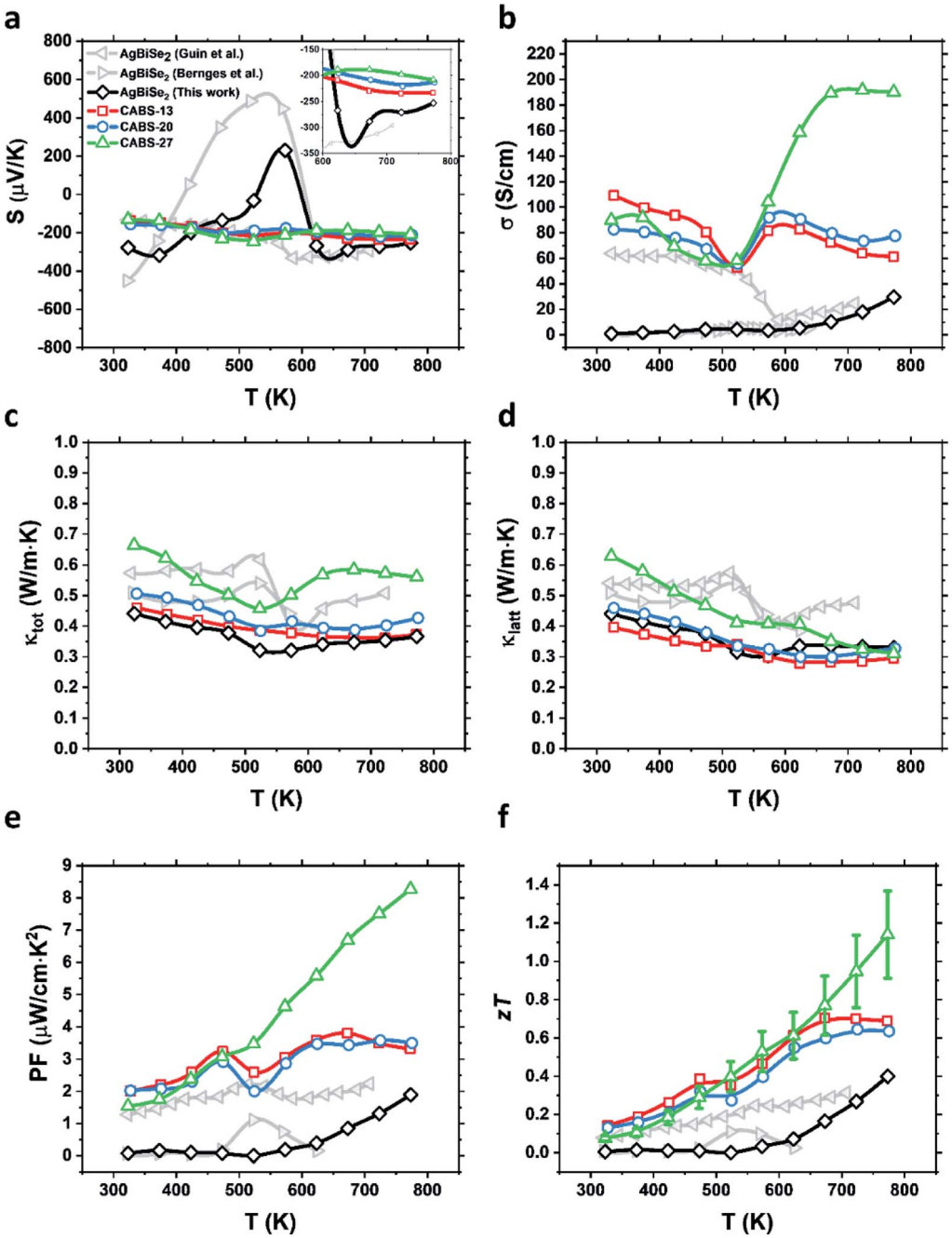

Fig. 3 TE Properties of CABS alloys. Temperature-dependent (a) Seebeck coefficient, (b) electrical conductivity, (c) power factor, (d) total thermal conductivity, (e) lattice thermal conductivity, and (f) dimensionless figure of merit (zT) of CABS-m. Identical symbols and colors indicate identical Cu concentrations (m values). The reported value of pristine ABS from the literature is plotted together for comparison. The uncertainty (error bar) of the zT measurement, ~15%, is only shown for CABS-27 for clarity.

a group of degenerate conduction bands forms near the CBM in CBS. This feature may originate from the relatively low energy of the Cu 4s orbital relative to that of the Ag 5s orbital, possibly forming lower energy states than Ag. Therefore, it is strongly suspected that CABS-27 possesses multiple degenerate bands – or nested bands – at the T point. These bands with high valley degeneracy would facilitate a high power factor by increasing the density-of-states (DOS) effective mass (m^*_{DOS}) without deteriorating the electrical conductivity.[21,41,43] Comparing Pisarenko plots at room temperature (see Fig. S9 in the ESI†) and at high temperatures (Fig. 1b) further demonstrates that band nestification occurs only after a phase transition.

To evaluate the beneficial effect of band nestification on the TE properties quantitatively, we estimated PF with Boltzmann transport equations in which a rigid band and constant relaxation-time approximation were assumed. The Fermi level was determined from the experimentally measured carrier concentration for ABS. For CABS and CBS, though the

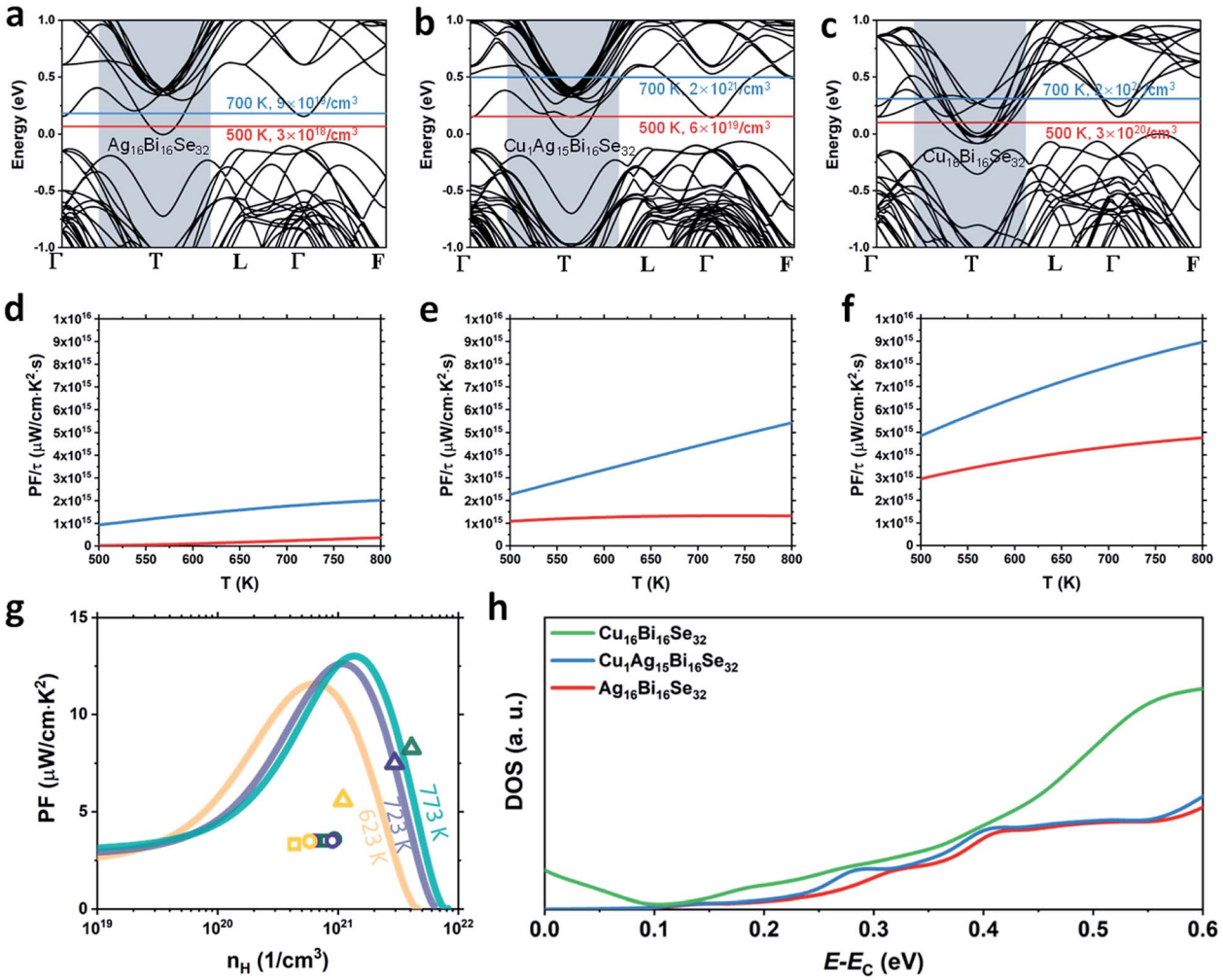

Fig. 4 Effect of nested bands on PF in the CABS system. (a–f) Calculated electronic band structures of $Ag_{16}Bi_{16}Se_{32}$, $Cu_1Ag_{15}Bi_{16}Se_{32}$, and $Cu_{16}Bi_{16}Se_{32}$ supercells with the $L1_1$ (AF-II) structure. The locations of the Fermi level at 500 K and 700 K are depicted by the red and blue lines, respectively. (d–f) Calculated ratios of the power factor to the relaxation time of $Ag_{16}Bi_{16}Se_{32}$, $Cu_1Ag_{15}Bi_{16}Se_{32}$, and $Cu_{16}Bi_{16}Se_{32}$ supercells for each Fermi level as determined by solving the Boltzmann transport equation. Identically colored lines depict an identical Fermi level in (a–c). (g) PF *versus* the carrier concentration for CABS alloys. Squares, circles, and triangles indicate the values for CABS-13, CABS-20, and CABS-27, respectively. Solid curves were fitted with the three-band model. (h) The calculated density of states of the conduction bands for the $Ag_{16}Bi_{16}Se_{32}$, $Cu_1Ag_{15}Bi_{16}Se_{32}$, and $Cu_{16}Bi_{16}Se_{32}$ supercell with the $L1_1$ structure.

compositions differ between the modelling and the experiment, the measured concentration was used to determine the Fermi level. As shown in Fig. 4d–f, PF of CABS and CBS is larger than that of ABS. Because we assumed a constant relaxation time and did not determine its value, the estimated PF reflects the effect of the electronic structure on the transport properties without considering the amount of scattering. In addition to the qualitative expectation from the band structure, the quantitative analysis with the Boltzmann transport equation supports the contention that the PF value can be increased with Cu doping due to band nestification. Comparing the measured electrical conductivity to the σ/τ value yields a relaxation time of $\sim 10^{-14}$ s, comparable to that of Bi_2Te_3[69–71] or PbTe.[72,73]

Fig. 4g shows the calculated power factor *versus* the carrier concentration with the three-band model with experimental data for various temperatures. While CABS-13 and CABS-20 are out of the fitted curve and far below the expected value, CABS-27 lies on the theoretical line. Although other sets of parameters may exist, this deviation implies that the electronic structures of CABS-13 and CABS-20 would be different from that of CABS-27. Moreover, the Hall carrier concentration at a high temperature is the highest in CABS-27 with a high Seebeck coefficient, an outcome attributed to the high DOS effective mass due to the increased valley degeneracy. The calculated DOS in Fig. 4h clearly shows the increased DOS with an increase in the Cu content, indicative of an increment in the DOS effective mass. Therefore, it is shown that the increase of m^*_{DOS} is indeed beneficial for improving TE properties in CABS system. Moreover, we confirmed the stability and the repeatability of the TE properties of CABS-27 by measuring them during three heating cycles (see Fig. S10 and S11 in the ESI†). These results emphasize that the overall TE properties, especially the high PF values,

are consistently stable, which is essential for long-term operation in actual power generation applications.

Conclusions

In summary, we demonstrated improved TE properties by inducing band nestification in $AgBiSe_2$-related materials for the first time, leading to an unprecedented high PF value of 8.2 μW cm^{-1} K^{-2} at 773 K. Consequently, a high zT_{max} value of 1.14 with a zT_{avg} value of 0.5 was achieved at 773 K, representing one of the highest values among $AgBiSe_2$-based TE materials. An additional reduction of the lattice thermal conductivity by constructing nanostructures or hierarchical architectures or optimization of the carrier concentration can be expected to further improve the TE performance capabilities of CABS alloys. Due to the low solubility and phase stability of $CuBiSe_2$ (see Fig. S14 in the ESI†), determining the TE properties of CABS alloys with a high Cu concentration beyond $m = 30$ remains an intriguing future work. Nonetheless, our fundamental understanding of the electronic band structure and conduction mechanism represents a significant advance in the development of high-performance, cost-effective, and environmentally benign TE materials.

Experimental section

Sample preparation

In this work, we prepared three samples with different Cu concentrations, with which Cu was intended to occupy Ag sites. For example, the chemical composition of CABS-13 is $Cu_{0.13}Ag_{0.87}BiSe_2$. Polycrystalline CABS-m samples ($m = 13$, 20, and 27) were synthesized by the melting and solidification method. High-purity elemental Ag shots (99.99%, Alfa Aesar), Bi shots (99.999%, 5N Plus), Se shots (99.999%, 5N Plus), and Cu pellets (99.997%, Yoochang Metal) were weighed according to the stoichiometric ratio. The raw materials were put into a quartz tube, and the tube was flame-sealed under a high vacuum of 10^{-5} Torr. Melting was done in a tube furnace at 1273 K for six hours, with further annealing at 773 K for 12 hours to homogenize the material. The ingot was pulverized into powder with an agate mortar and densified by spark plasma sintering (Dr Sinter SPS-211, Fuji Electronic Industrial) at 773 K for ten minutes under pressure of 10^{-3} Torr. A graphite mold and a punch with a diameter of 12.7 mm were used during the sintering process. All samples exhibited a high relative density of approximately 99% of the theoretical density.

Characterization

Structural and crystallographic characterization assessments were conducted by X-ray diffractometry with a CuK_α radiation source (SmartLab, Rigaku) from 20° to 80° with a step size of 0.01° and a scan speed of 2° per minute. Powders with particle sizes of less than approximately 45 μm were used for PXRD measurements. The high-temperature X-ray diffraction pattern was acquired under an N_2 atmosphere with a heating rate of 5 K min^{-1}. A platinum (Pt) holder was used to prevent a reaction between the sample and the holder. The microstructures of the fracture surface and the polished surface were analyzed using a field-emission scanning electron microscope (FE-SEM S-4800, Hitachi). Elemental mapping of the polished surface was conducted using an energy-dispersive X-ray spectrometer (EMAX, Horiba) equipped in a FE-SEM device. The characteristics of the lattice dynamics were investigated by transmission electron microscopy (Tecnai F30, FEI), and the bonding states of the element were investigated by means of *in situ* X-ray photoelectron spectroscopy (Axis-Supra, Kratos). The optical band gap was measured by diffuse reflectance spectroscopy (DRS) with UV-vis spectrometer (Lambda 1050, PerkinElmer). Temperature-dependent Hall measurements were conducted with the van-der-Pauw method with four tungsten contacts under a magnetic field of 0.5 T (ResiTest 8300, TOYO Corporation).

Thermoelectric property measurements

Sintered samples were mechanically cut into round (ø 12.7 × 1 mm^3) and bar-shape (3 × 3 × 10 mm^3) specimens for thermal and electronic transport property measurements, respectively. All TE properties were measured along the same direction (parallel to the press direction) to minimize any possible error due to the anisotropy of the material. The temperature-dependent electrical conductivity and Seebeck coefficient were simultaneously measured in a He atmosphere with a commercial apparatus (BS-1, Bluesys). The thermal conductivity was calculated *via* $\kappa = \rho C_p D$, where ρ is the bulk density, C_p is the heat capacity, and D is the thermal diffusivity of the material. The bulk density was measured by the Archimedes method, and the heat capacity was calculated using the Dulong–Petit law.[37,38] The thermal diffusivity was measured using a laser flash apparatus (LFA 457, NETZSCH) under an Ar atmosphere. The weighted mobility was calculated using Drude-Sommerfeld free electron model.[74] The Lorenz number was obtained from the Seebeck coefficient based on the assumption of a single parabolic band.[75]

Computational details

First-principles calculations were performed based on the density functional theory (DFT) with the generalized gradient approximation (GGA) as parameterized by Perdew, Burke, and Ernzerhof (PBE), implemented in the Vienna *ab initio* simulation package (VASP) code.[76–78] We used the projector augmented wave (PAW) pseudopotential for the valence and the ionic core interactions.[79] The disordering of cations between Ag and Bi for the cubic phase of ABS at high temperatures can be described with mixture of the ordered AF-II ($L1_1$) and AF-IIb ($D4$) structures. Hence, the electronic structures of the ordered $L1_1$ and $D4$ structures were evaluated to consider the disordering of cations of ABS. To model both $L1_1$ and $D4$ cubic structures for ABS, the NaCl-type cell with alternating Ag–Se planes and Bi–Se planes normal to the [100] direction was doubled along all three directions while the cations were rearranged. Due to this rearrangement of cations, there is no symmetric relationship with the original NaCl-type cell and the cell with 64 atoms. Thus, we

could not unfold the band structure because the cubic cell is the original cell itself.[80] As a result, the supercell with 64 atoms is essentially needed for $L1_1$ and $D4$ cubic structures of ABS. The supercells with 64 atoms were used in the total energy calculations for cubic structures of ABS, CABS, and CBS and the Brillouin zone was not unfolded. An energy cutoff of 350 eV and a 6 × 6 × 6 gamma-centered *k*-points mesh were used. The lattice parameter and the internal atomic positions were fully relaxed until the forces were within 0.02 eV $Å^{-1}$ for each atom. The spin orbital interaction (SOI) is included in all calculations, except for the structure optimization. Electronic transport properties were calculated with the BoltzTraP2 code.[81]

Author contributions

H. Jang, S. Abbey, B. Frimpong, C. V. Nguyen, H. S. Shin, and J. Y. Song synthesized and measured TE properties of CABS alloys. W. H. Nam conducted high-temperature Hall measurements. M. W. Oh conducted DFT calculations. M. W. Oh and Y. S. Jung supervised the work. All authors participated to the discussion of the results and writing of the manuscript.

Conflicts of interest

There are no conflicts to declare.

Acknowledgements

This work was supported by the Creative Materials Discovery Program through the National Research Foundation of the Republic of Korea (NRF) funded by Ministry of Science and ICT (No. 2020M3D1A1110501).

Notes and references

1 G. J. Snyder and E. S. Toberer, *Nat. Mater.*, 2008, **7**, 105–114.
2 F. J. DiSalvo, *Science*, 1999, **285**, 703–706.
3 S. I. Kim, K. H. Lee, H. A. Mun, H. S. Kim, S. W. Hwang, J. W. Roh, D. J. Yang, W. H. Shin, X. S. Li, Y. H. Lee, G. J. Snyder and S. W. Kim, *Science*, 2015, **348**, 109–114.
4 R. J. Mehta, Y. Zhang, C. Karthik, B. Singh, R. W. Siegel, T. Borca-Tasciuc and G. Ramanath, *Nat. Mater.*, 2012, **11**, 233–240.
5 S. Seo, K. Lee, Y. Jeong, M. W. Oh and B. Yoo, *J. Phys. Chem. C*, 2015, **119**, 18038–18045.
6 L. Yue, T. Fang, S. Q. Zheng, W. L. Cui, Y. Wu, S. Y. Chang, L. J. Wang, P. P. Bai and H. Z. Zhao, *ACS Appl. Energy Mater.*, 2019, **2**, 2596–2603.
7 H. S. Lee, B. S. Kim, C. W. Cho, M. W. Oh, B. K. Min, S. D. Park and H. W. Lee, *Acta Mater.*, 2015, **91**, 83–90.
8 J. Tang, B. Gao, S. Q. Lin, X. Wang, X. Y. Zhang, F. Xiong, W. Li, Y. Chen and Y. Z. Pei, *ACS Appl. Energy Mater.*, 2018, **3**, 1969–1974.
9 L. Wang, X. J. Tan, G. Q. Liu, J. T. Xu, H. Z. Shao, B. Yu, H. C. Jiang, S. Yue and J. Jiang, *ACS Appl. Energy Mater.*, 2017, **2**, 1203–1207.
10 L. L. Zheng, W. Li, S. Q. Lin, J. Li, Z. W. Chen and Y. Z. Pei, *ACS Appl. Energy Mater.*, 2017, **2**, 563–568.
11 J. Ma, O. Delaire, A. F. May, C. E. Carlton, M. A. McGuire, L. H. VanBebber, D. L. Abernathy, G. Ehlers, T. Hong, A. Huq, W. Tian, V. M. Keppens, Y. Shao-Horn and B. C. Sales, *Nat. Nanotechnol.*, 2013, **8**, 445–451.
12 B. L. Du, H. Li, J. J. Xu, X. F. Tang and C. Uher, *Chem. Mater.*, 2010, **22**, 5521–5527.
13 J. K. Lee, M. W. Oh, B. Ryu, J. E. Lee, B. S. Kim, B. K. Min, S. J. Joo, H. W. Lee and S. D. Park, *Sci. Rep.*, 2017, **7**, 4496.
14 Y. H. Ko, M. W. Oh, J. K. Lee, S. D. Park, K. J. Kim and Y. S. Choi, *Curr. Appl. Phys.*, 2014, **14**, 1538–1542.
15 Y. He, T. S. Zhang, X. Shi, S. H. Wei and L. D. Chen, *NPG Asia Mater.*, 2015, **7**, e210.
16 Z. X. Ye, J. Y. Cho, M. M. Tessema, J. R. Salvador, R. A. Waldo, H. Wang and W. Cai, *J. Solid State Chem.*, 2013, **201**, 262–269.
17 K. Zhao, K. Liu, Z. Yue, Y. Wang, Q. Song, J. Li, M. Guan, Q. Xu, P. Qiu, H. Zhu, L. Chen and X. Shi, *Adv. Mater.*, 2019, **31**, 1903480.
18 Y. Luo, S. Cai, S. Hao, F. Pielnhofer, I. Hadar, Z.-Z. Luo, J. Xu, C. Wolverton, V. P. Dravid, A. Pfitzner, Q. Yan and M. G. Kanatzidis, *Joule*, 2020, **4**, 159–175.
19 C. Han, G. J. Tan, T. Varghese, M. G. Kanatzidis and Y. L. Zhang, *ACS Appl. Energy Mater.*, 2018, **3**, 818–822.
20 S. Sarkar, X. M. Zhang, S. Q. Hao, X. Hua, T. P. Bailey, C. Uher, C. Wolverton, V. P. Dravid and M. G. Kanatzidis, *ACS Appl. Energy Mater.*, 2018, **3**, 2593–2601.
21 Y. Pei, H. Wang and G. J. Snyder, *Adv. Mater.*, 2012, **24**, 6125–6135.
22 D. L. Anderson, *Theory of the earth*, Blackwell Scientific, 1989.
23 L. D. Zhao, S. H. Lo, Y. Zhang, H. Sun, G. Tan, C. Uher, C. Wolverton, V. P. Dravid and M. G. Kanatzidis, *Nature*, 2014, **508**, 373–377.
24 L. D. Zhao, G. Tan, S. Hao, J. He, Y. Pei, H. Chi, H. Wang, S. Gong, H. Xu, V. P. Dravid, C. Uher, G. J. Snyder, C. Wolverton and M. G. Kanatzidis, *Science*, 2016, **351**, 141–144.
25 H. Liu, X. Shi, F. Xu, L. Zhang, W. Zhang, L. Chen, Q. Li, C. Uher, T. Day and G. J. Snyder, *Nat. Mater.*, 2012, **11**, 422–425.
26 H. Liu, X. Yuan, P. Lu, X. Shi, F. Xu, Y. He, Y. Tang, S. Bai, W. Zhang, L. Chen, Y. Lin, L. Shi, H. Lin, X. Gao, X. Zhang, H. Chi and C. Uher, *Adv. Mater.*, 2013, **25**, 6607–6612.
27 Y. K. Lee, Z. Luo, S. P. Cho, M. G. Kanatzidis and I. Chung, *Joule*, 2019, **3**, 719–731.
28 S. Chandra and K. Biswas, *J. Am. Chem. Soc.*, 2019, **141**, 6141–6145.
29 C. L. Chen, H. Wang, Y. Y. Chen, T. Day and G. J. Snyder, *J. Mater. Chem. A*, 2014, **2**, 11171–11176.
30 G. Dennler, R. Chmielowski, S. Jacob, F. Capet, P. Roussel, S. Zastrow, K. Nielsch, I. Opahle and G. K. H. Madsen, *Adv. Energy Mater.*, 2014, **4**, 1301581.
31 S. N. Guin, A. Chatterjee, D. S. Negi, R. Datta and K. Biswas, *Energy Environ. Sci.*, 2013, **6**, 2603–2608.
32 S. N. Guin, D. S. Negi, R. Datta and K. Biswas, *J. Mater. Chem. A*, 2014, **2**, 4324–4331.

33 E. Rathore, R. Juneja, S. P. Culver, N. Minafra, A. K. Singh, W. G. Zeier and K. Biswas, *Chem. Mater.*, 2019, **31**, 2106–2113.
34 H. J. Wu, P. C. Wei, H. Y. Cheng, J. R. Deng and Y. Y. Chen, *Acta Mater.*, 2017, **141**, 217–229.
35 Y. Goto, A. Nishida, H. Nishiate, M. Murata, C. H. Lee, A. Miura, C. Moriyoshi, Y. Kuroiwa and Y. Mizuguchi, *Dalton Trans.*, 2018, **47**, 2575–2580.
36 T. Bernges, J. Peilstocker, M. Dutta, S. Ohno, S. P. Culver, K. Biswas and W. G. Zeier, *Inorg. Chem.*, 2019, **58**, 9236–9245.
37 S. N. Guin, V. Srihari and K. Biswas, *J. Mater. Chem. A*, 2015, **3**, 648–655.
38 L. Pan, D. Berardan and N. Dragoe, *J. Am. Chem. Soc.*, 2013, **135**, 4914–4917.
39 M. M. Zou, Q. Liu, C. F. Wu, T. R. Wei, Q. Tan, J. F. Li and F. Chen, *RSC Adv.*, 2018, **8**, 7055–7061.
40 M. D. Nielsen, V. Ozolins and J. P. Heremans, *Energy Environ. Sci.*, 2013, **6**, 570–578.
41 Y. Pei, X. Shi, A. LaLonde, H. Wang, L. Chen and G. J. Snyder, *Nature*, 2011, **473**, 66–69.
42 L. D. Zhao, H. J. Wu, S. Q. Hao, C. I. Wu, X. Y. Zhou, K. Biswas, J. Q. He, T. P. Hogan, C. Uher, C. Wolverton, V. P. Dravid and M. G. Kanatzidis, *Energy Environ. Sci.*, 2013, **6**, 3346–3355.
43 K. Imasato, S. D. Kang, S. Ohno and G. J. Snyder, *Mater. Horiz.*, 2018, **5**, 59–64.
44 W. He, D. Wang, H. Wu, Y. Xiao, Y. Zhang, D. He, Y. Feng, Y.-J. Hao, J.-F. Dong, R. Chetty, L. Hao, D. Chen, J. Qin, Q. Yang, X. Li, J.-M. Song, Y. Zhu, W. Xu, C. Niu, X. Li, G. Wang, C. Liu, M. Ohta, S. J. Pennycook, J. He, J.-F. Li and L.-D. Zhao, *Science*, 2019, **365**, 1418–1424.
45 S. Lin, W. Li, Z. Chen, J. Shen, B. Ge and Y. Pei, *Nat. Commun.*, 2016, **7**, 10287.
46 M. Mukherjee, G. Yumnam and A. K. Singh, *J. Phys. Chem. C*, 2018, **122**, 29150–29157.
47 H.-S. Kim, N. A. Heinz, Z. M. Gibbs, Y. Tang, S. D. Kang and G. J. Snyder, *Mater. Today*, 2017, **20**, 452–459.
48 W. Liu, X. Tan, K. Yin, H. Liu, X. Tang, J. Shi, Q. Zhang and C. Uher, *Phys. Rev. Lett.*, 2012, **108**, 166601.
49 K. Sudo, Y. Goto, R. Sogabe, K. Hoshi, A. Miura, C. Moriyoshi, Y. Kuroiwa and Y. Mizuguchi, *Inorg. Chem.*, 2019, **58**, 7628–7633.
50 Y. D. Guan, Y. Huang, D. Wu, D. Feng, M. K. He and J. Q. He, *Appl. Phys. Lett.*, 2018, **112**, 213905.
51 Y.-L. Pei, H. Wu, J. Sui, J. Li, D. Berardan, C. Barreteau, L. Pan, N. Dragoe, W.-S. Liu, J. He and L.-D. Zhao, *Energy Environ. Sci.*, 2013, **6**, 1750–1755.
52 Z. Feng, X. Zhang, Y. Wang, J. Zhang, T. Jia, B. Cao and Y. Zhang, *Phys. Rev. B*, 2019, **99**, 155203.
53 J. Z. Xin, Y. L. Tang, Y. T. Liu, X. B. Zhao, H. G. Pan and T. J. Zhu, *npj Quantum Mater.*, 2018, **3**, 9.
54 C. Xiao, X. Qin, J. Zhang, R. An, J. Xu, K. Li, B. Cao, J. Yang, B. Ye and Y. Xie, *J. Am. Chem. Soc.*, 2012, **134**, 18460–18466.
55 K. Hoang, S. D. Mahanti, J. R. Salvador and M. G. Kanatzidis, *Phys. Rev. Lett.*, 2007, **99**, 156403.
56 T. Pandey, A. S. Nissimagoudar, A. Mishra and A. K. Singh, *J. Mater. Chem. A*, 2020, **8**, 13812–13819.
57 H. Peng, N. Kioussis and D. A. Stewart, *Appl. Phys. Lett.*, 2015, **107**, 251904.
58 M. Dutta, K. Pal, U. V. Waghmare and K. Biswas, *Chem. Sci.*, 2019, **10**, 4905–4913.
59 M. K. Jana and K. Biswas, *ACS Appl. Energy Mater.*, 2018, **3**, 1315–1324.
60 P. G. Klemens, *Phys. Rev.*, 1960, **119**, 507–509.
61 K. Imasato, S. D. Kang and G. J. Snyder, *Energy Environ. Sci.*, 2019, **12**, 965–971.
62 C. Stavrakas, S. J. Zelewski, K. Frohna, E. P. Booker, K. Galkowski, K. Ji, E. Ruggeri, S. Mackowski, R. Kudrawiec, P. Plochocka and S. D. Stranks, *Adv. Energy Mater.*, 2019, **9**, 1901883.
63 C. L. Mao, S. G. Yan, S. Cao, C. H. Yao, F. Cao, G. S. Wang, X. L. Dong, X. Hu and C. L. Yang, *J. Eur. Ceram. Soc.*, 2014, **34**, 2933–2939.
64 R. He, D. Kraemer, J. Mao, L. Zeng, Q. Jie, Y. Lan, C. Li, J. Shuai, H. S. Kim, Y. Liu, D. Broido, C.-W. Chu, G. Chen and Z. Ren, *Proc. Natl. Acad. Sci. U. S. A.*, 2016, **113**, 13576.
65 M. W. Oh, D. M. Wee, S. D. Park, B. S. Kim and H. W. Lee, *Phys. Rev. B: Condens. Matter Mater. Phys.*, 2008, **77**, 165119.
66 K. Hoang and S. D. Mahanti, *Journal of Science: Advanced Materials and Devices*, 2016, **1**, 51–56.
67 H. Xiao, J. Tahir-Kheli and W. A. Goddard, *J. Phys. Chem. Lett.*, 2011, **2**, 212–217.
68 J. P. Perdew, W. Yang, K. Burke, Z. Yang, E. K. U. Gross, M. Scheffler, G. E. Scuseria, T. M. Henderson, I. Y. Zhang, A. Ruzsinszky, H. Peng, J. Sun, E. Trushin and A. Görling, *Proc. Natl. Acad. Sci. U. S. A.*, 2017, **114**, 2801–2806.
69 N. F. Hinsche, B. Y. Yavorsky, I. Mertig and P. Zahn, *Phys. Rev. B: Condens. Matter Mater. Phys.*, 2011, **84**, 165214.
70 C. Lee, J. N. Kim, J.-Y. Tak, H. K. Cho, J. H. Shim, Y. S. Lim and M.-H. Whangbo, *AIP Adv.*, 2018, **8**, 115213.
71 J. Liang, L. Cheng, J. Zhang, H. Liu and Z. Zhang, *Nanoscale*, 2016, **8**, 8855–8862.
72 S. Ahmad and S. D. Mahanti, *Phys. Rev. B: Condens. Matter Mater. Phys.*, 2010, **81**, 165203.
73 D. I. Bilc, S. D. Mahanti and M. G. Kanatzidis, *Phys. Rev. B: Condens. Matter Mater. Phys.*, 2006, **74**, 125202.
74 G. J. Snyder, A. H. Snyder, M. Wood, R. Gurunathan, B. H. Snyder and C. Niu, *Adv. Mater.*, 2020, **32**, e2001537.
75 H.-S. Kim, Z. M. Gibbs, Y. Tang, H. Wang and G. J. Snyder, *APL Mater.*, 2015, **3**, 041506.
76 J. P. Perdew, K. Burke and M. Ernzerhof, *Phys. Rev. Lett.*, 1996, **77**, 3865–3868.
77 G. Kresse and J. Hafner, *Phys. Rev. B: Condens. Matter Mater. Phys.*, 1993, **47**, 558–561.
78 G. Kresse and J. Hafner, *Phys. Rev. B: Condens. Matter Mater. Phys.*, 1994, **49**, 14251–14269.
79 G. Kresse and D. Joubert, *Phys. Rev. B: Condens. Matter Mater. Phys.*, 1999, **59**, 1758–1775.
80 In order to unfold the band structure of the cubic cell, we need to model a new enlarged cell. For example, the primitive cell of the cubic $L1_1$ structure for ABS($Ag_{16}Bi_{16}Se_{32}$) is hexagonal cell with the composition of $Ag_3Bi_3Se_6$. In order to get the unfolded band structure, we should make an enlarged cell from this hexagonal cell. In

order to make the Cu-dopped ABS with the same composition of the $Cu_1Ag_{15}Bi_{16}Se_{32}$, the enlarged cell with the composition of $Cu_3Ag_{45}Bi_{48}Se_{96}$ was constructed. If we can get the electronic structure of $Cu_3Ag_{45}Bi_{48}Se_{96}$, the unfolded band structure, based on the primitive hexagonal cell, can be compared with that of $Ag_3Bi_3Se_6$. However, it was impossible to get the electronic structure of the cell with 192 atoms including spin orbital interaction.

81 G. K. H. Madsen, J. Carrete and M. J. Verstraete, *Comput. Phys. Commun.*, 2018, **231**, 140–145.